Fourier Mode Decomposition of Unsteady Flows in a Single Injection Port Fluidic Thrust Vectoring Nozzle

Jianming Wang[1] · Siqi Luan[1] · Jianyong Zhu[1] · Xiaodong Mao[1] · Junqiang Wu[2]

Abstract

The flow field structure of a single injection port fluidic thrust vectoring nozzle was studied by introducing secondary flow injection in the expansion section of the two-dimensional convergent-divergent nozzle. To determine the motion characteristics of unsteady flow in a shock-induced fluidic vectoring nozzle, detached eddy simulation was conducted to simulate the three-dimensional flow field, and the flow mechanism in the nozzle was analyzed. Fourier mode decomposition was used to analyze the pressure coefficient on the symmetrical surface of the nozzle. Results show three natural frequencies in the flow field of the shock-induced fluidic vectoring nozzle. The first-order mode corresponding to frequency $f_1 = 512.8$ Hz mainly illustrates the oscillation of shock waves. The second-order mode corresponding to frequency $f_2 = 2825$ Hz illustrates the shedding of vortices. The third-order mode corresponding to frequency $f_3 = 4650$ Hz is similar to the second-order mode; however, the spatial scales of vortices decrease.

Keywords Fluidic thrust vectoring nozzle · Shock wave · Flow structure · Fourier mode decomposition

1 Introduction

Thrust vectoring can effectively improve the engine's performance, which has become an interesting research topic recently [1, 2]. The principle of thrust vectoring is to manipulate and control the aircraft by changing the flow direction of the engine tail nozzle. Thrust vectoring can considerably reduce the take-off and landing glide distances of the aircraft. The engine tail nozzle is the key component to realize thrust vectoring. The thrust vectoring nozzle can be classified into mechanical thrust vectoring nozzles and fluidic thrust vectoring nozzles. The mechanical vectoring nozzle has already been used in the military, and maintaining this nozzle is difficult because of its heavyweight and complex structure [3]. Additionally, the thrust loss of engine is too large. When the engine tail nozzle is in the non-mechanical deflection condition, the fluidic thrust vectoring nozzle controls the main flow direction by controlling gas flow and then obtains the control force and control torque required for flight control [4]. Compared with the mechanical thrust vectoring nozzle, the fluidic thrust vectoring nozzle has the advantages of low weight, simple structure, and low maintenance cost [5]. On the basis of different control principles, several control methods can be used for fluidic thrust vectoring, including the dual throat nozzle [6], co-flow method [7], shock vector control [8], etc. Shock vector control has a very short response time, which is an ideal design scheme [9].

Giuliano et al. conducted an experimental investigation of a hexagonal flow path convergent–divergent nozzle with a fluidic injection for thrust vectoring and expansion control [10]. The experiment controlled the direction change of a jet (pitch/yaw) by arranging secondary jet slots on the wall of the nozzle expansion section (upper and lower wall/sidewall). Test results indicated the thrust vectoring of up to 15° in pitch or yaw, up to 10° in simultaneous pitch and yaw, and thrust performance within 3%–4% of a conventional variable geometry nozzle at low power. Wing et al. experimented on an axisymmetric vector nozzle with fluidic injection and studied the effects of different injection-port geometry and location on thrust vectoring [11]. Computational fluid

✉ Jianming Wang
jmwang_sau@163.com

✉ Junqiang Wu
junqiangwu_cardc@163.com

1 Liaoning Key Lab of Advanced Test Technology for Aerospace Propulsion, College of Aeroengine, Shenyang Aerospace University, Shenyang 110136, China

2 China Aerodynamics Research and Development Center, Mianyang 621000, China

dynamics code PAB was used by Deere to study the aerodynamic effects on fluidic thrust vectoring [12], in which it was found that the freestream flow causes the shock wave to move upstream, thereby reducing the vector angle and thrust efficiency. Waithe et al. studied the fluid thrust vectoring of a two-dimensional convergent–divergent (2DCD) vectoring nozzle under one injection port or multiple injection ports [13], experimental results illustrate that the multiple injection ports' jet effect is better than that of the one injection port when the nozzle pressure ratio is less than 4 with high secondary pressure ratio. An experimental and numerical study of the fluidic thrust vectoring of a 2D supersonic nozzle was conducted by changing the injection mass flow rate and nozzle pressure ratio, and the obtained findings show that shock vector control is the most efficient when the nozzle is under expanded [14].

Previous researches on nozzles mainly focus on the efficiency of thrust vectoring. The unsteady structure and the spectral characteristics of the flow field need to be further studied. Fourier mode decomposition (FMD) is an advanced flow field analysis method. Ma et al. proposed this method and used FMD technology to obtain the natural frequency and driving frequency of the flow field; they further obtained dynamic information such as amplitude and phase [15]. The FMD technique will be used to decompose and analyze the flow field of the nozzle in this paper. Thereafter, the frequency characteristics of the unsteady oscillation flow field, the oscillation law, and potential dynamics information corresponding to each frequency are obtained. The details of FMD will be explained in the third chapter.

2 Computational Model and Setup

2.1 Computational Model and Grids

Numerical simulation is conducted using the experimental configuration in reference [13]. A non-axisymmetric, 2DCD nozzle is used in this paper, with the throat area of 2.785×10^{-3} m^2. The calculation domain and grids are shown in Fig. 1. The "+" in Fig. 1b is the coordinate origin, and it is located at the center of the primary flow inlet. The primary flow moves along the X axis. Considering the influence of the external field on the reliability of the calculation results, the width and height of the external flow field are three and six times the nozzle outlet size, and the length is 10 times the nozzle length. The structured grids are applied to the entire flow field with a total number of approximately 2.5 million. The grids are partially refined at the secondary flow inlet,

Fig. 1 Computational domain and grids

(a) Computational grids

(b) Zoomed-in grids

(c) Secondary flow ejector grids
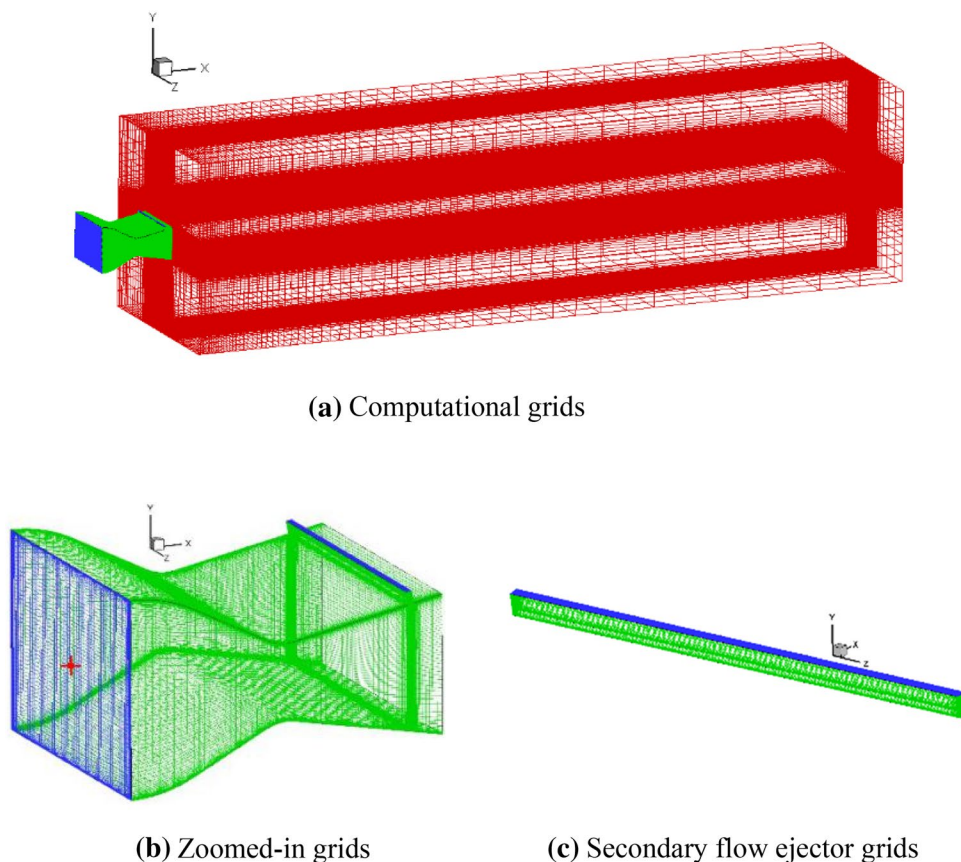
and the outer flow field grids are gradually sparse along the X axis. The y$^+$ of the first cell of the wall is less than 1.

2.2 Computational Setup

Same as reference [16–19], FLUENT software is used for the numerical calculation in this paper. The DES is a form of hybrid large eddy simulation (LES)/ Reynolds-averaged Navier–Stokes (RANS) turbulence modelling, and its basic idea is to employ an unsteady RANS approach in the boundary layer and LES treatment in the separation regions and primary flow [20]. The DES involves a small amount of calculation and has good simulation ability for flow separation and unsteady characteristics. The SST k-ω DDES turbulence model of fluent software is used to solve the unsteady flow, detailed equation of DES can be referred to in references [21, 22]. Nozzle pressure ratio (NPR) is the ratio of primary flow total pressure to atmospheric pressure. Secondary pressure ratio (SPR) is the ratio of the total pressure of secondary flow to the primary flow total pressure. In this paper, NPR is 4.6, SPR is 0.7, the outlet static pressure is 101,325 Pa, and the total temperature of both outlet and inlet is 300 K. The time step size is 5e-05 s. The total computational time length is 150 data cycles.

3 Fourier Mode Decomposition

FMD adopt the DFT-based method to extract the dominant information from the complex flow phenomena. Compared with dynamic mode decomposition (DMD) [23, 24], FMD saves computing time and reduces the computational difficulty. There are natural shedding frequencies and actuation frequencies in the flow field, FMD can extract dynamic information(pressure, velocity, density, etc.) at specific frequencies in the global power spectrum [15]. This method was proposed by MA LiQun [15], and then the principle and process of FMD will be explained in detail.

The calculated data are discrete, and the data of each point can be expressed as

$$F_n = \sum_{k=0}^{N-1} c_k e^{i\frac{2\pi k}{N}n},\tag{1}$$

where

$$c_k = \frac{1}{N}\sum_{n=0}^{N-1} F_n e^{-i\frac{2\pi k}{N}n}.\tag{2}$$

Equation (1) can be represented as $F_n = F(n\Delta t)$, Δt is the time interval, $\Delta t = 1/f_s$, f_s stands for the sampling frequency and N is the total sampling number. Generalization from the single point to the global flow field, then

$$\boldsymbol{F}_n = \mathbf{F}(n\Delta t),\tag{3}$$

$$\mathbf{c}_k = \frac{1}{N}\sum_{n=0}^{N-1} \mathbf{F}_n e^{-i\frac{2\pi k}{N}n}.\tag{4}$$

The bold $\boldsymbol{F}_n$ represents a matrix containing all the discrete data information of the time–space flow field, $\boldsymbol{c}_k$ in bold is a matrix sequence of global spectral information that is discretized in the frequency domain and can express as

$$\mathbf{c}_k = \frac{1}{2}\mathbf{A}_k e^{-i\theta_k} = \frac{1}{2}\mathbf{A}_k\left(\cos\theta_k - i\sin\theta_k\right),\tag{5}$$

$\mathbf{A_k}$ is the global amplitude spectrum and $\boldsymbol{\theta_k}$ is the global phase spectrum, where

$$\mathbf{A_k} = 2\left|\mathbf{c}_k\right|, \quad \boldsymbol{\theta}_k = -\arg\mathbf{c}_k.\tag{6}$$

Extracting the data of the same frequency of different discrete points from the matrix $\mathbf{c}_k$, the dynamic mode corresponding to this frequency is the Fourier mode.

Evolving the mode in the time domain, and the mode at the jth moment can be expressed as:

$$c_k^j = \mathbf{c}_k(e^{-i\theta_k})^{j-1}.\tag{7}$$

4 Results and Analysis of Calculation

4.1 Validation of the Calculation

In the numerical calculation process, the accuracy of the calculation results and the calculation speed must be ensured, so the number of grids is crucial. In this paper, four groups of grids are selected to test the grid independence, namely, 1.5, 2, 2.5, and 3 million. Figure 2 illustrates the pressure on the upper wall of the nozzle divergent section for different grid numbers. The horizontal axis is the axial position of the upper wall of the nozzle, and the vertical axis is the upper wall pressure. The pressure values of the wall with different grid numbers vary considerably. When the grids reach 2.5 million or more, the pressure value of the wall remains basically unchanged, so the calculated result will not change greatly as the grid number continues to increase. The calculation speed of the grids is also reasonable. Therefore, the number of grids used in this paper is 2.5 million.

In Fig. 3, the abscissa is the ratio of the axial coordinate X of the monitoring point to the position X_t of the nozzle throat position, and the ordinate is the ratio of the wall pressure value P of the monitoring point to the primary flow inlet pressure $P_{t,p}$ of the nozzle. As shown in Fig. 3, the calculated curve agrees well with the experimental data of the reference [13], so the calculation result is valid.
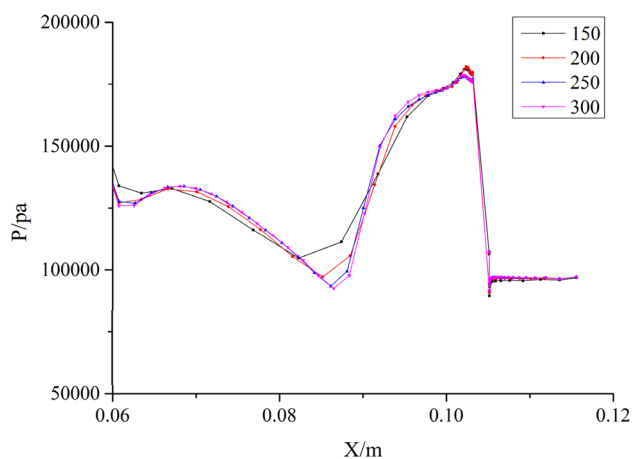
**Fig. 2** Pressure on the upper wall of the nozzle divergent section for different grid numbers

4.2 Flow Structure of Thrust Vectoring Nozzle

Secondary flow of the thrust vectoring nozzle comes from the compressor of the aeroengine. The secondary flow in the high-pressure under-expanded state from the nozzle divergent section will continue to expand when it flows into the supersonic primary flow. A certain jet depth will be formed in the primary flow, which blocks the primary flow and forms an induced shock wave. The static pressure of the primary flow after the induced shock wave rises sharply, forming adverse pressure gradient, which transmits along with the subsonic boundary layer to the front of the induced shock and makes the boundary layer thicker. Subsequently, the fluid refluxes to form a separation region, where the supersonic primary flow is compressed and a separation

shock wave is generated. Figure 4 shows that the primary flow has achieved effective vector deflection.

The separation shock wave intersects with the induced shock wave and is synthesized into a "λ" shock wave. The "λ" shock wave intersects the shear layer and reflects as an expansion wave. The expansion wave is reflected downstream on the free shear layer into a compression wave, and a cycle repeats. Given the viscous action of the gas, the wake and surrounding atmosphere continuously exchange mass and momentum. The kinetic energy continues to decrease, and the velocity of flow gradually falls; this phenomenon weakens until it disappears. The shear layers are formed at the interface of the upper and lower sides of the wake and the free flow due to the velocity difference and the shear action caused by the viscous flow. An oblique shock is found near the lower wall's lip of the nozzle. The primary flow here is over-expanded, the over-expanded airflow is compressed by the atmosphere, so the oblique shock wave is generated. The oblique shock wave intersects the separation shock wave and forms a fork-shaped shock wave distribution close to the lower shear layer.

Figure 5 shows the specific position of the y–z planes, which will be discussed in the following. Figure 6 is the flow field distribution of the nozzle 1/2 y–z plane whose position is shown in Fig. 5. The velocity vector is composed of Z-velocity and Y-velocity. Figure 6a shows that the flow field in the nozzle maintains quasi-2D flow upstream of the separation shock wave. The shock wave represented by the blue line can be clearly observed, and it deflects at the wall in Fig. 6. The deflection of the shock is caused by the intersection of the induced shock and the separation shock generated by the boundary layer separation at the sidewall. In Fig. 6c and d, a local high-speed region can be observed

(a) Upper wall

(b) Lower wall
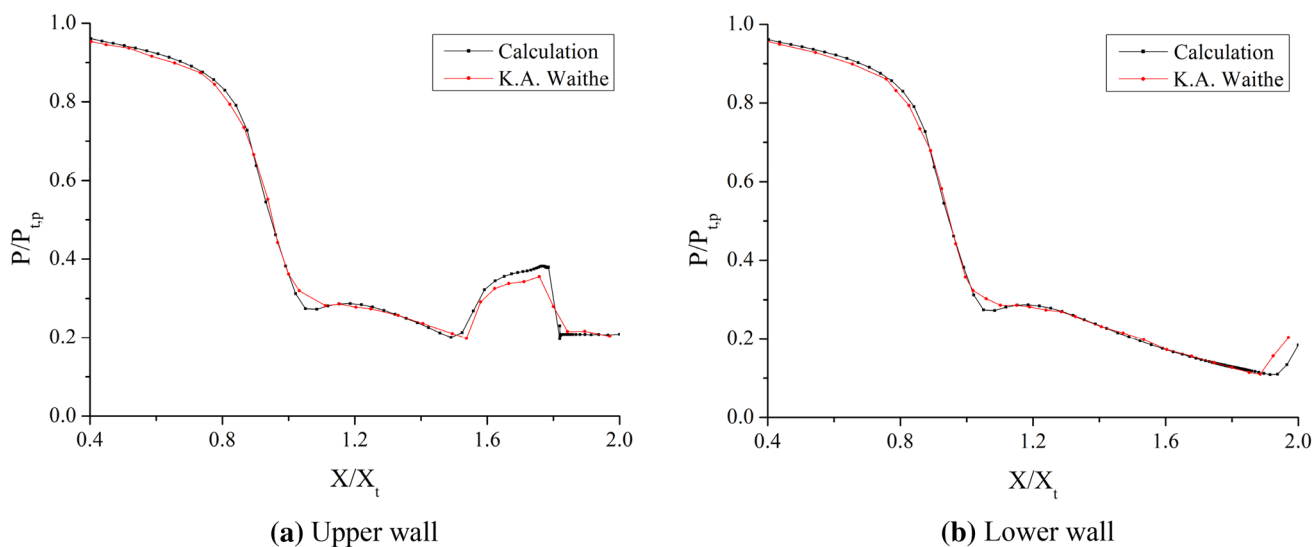
Fig. 3 Comparison of experimental results [13] with calculation results of pressure distribution
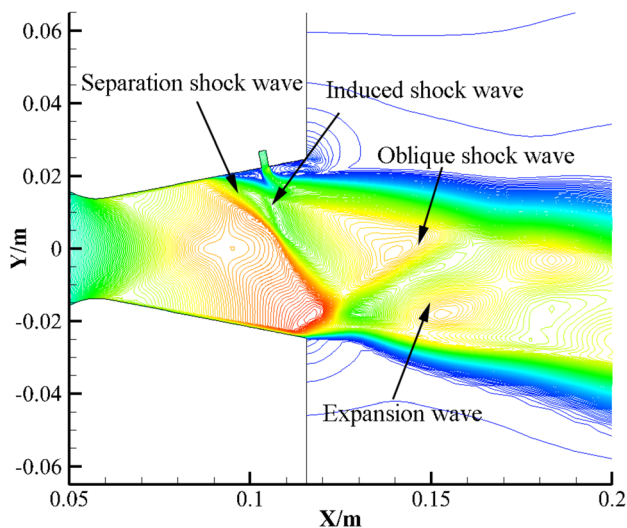
Fig. 4 Mach number contour of the nozzle's symmetry plane ($Z=0$)
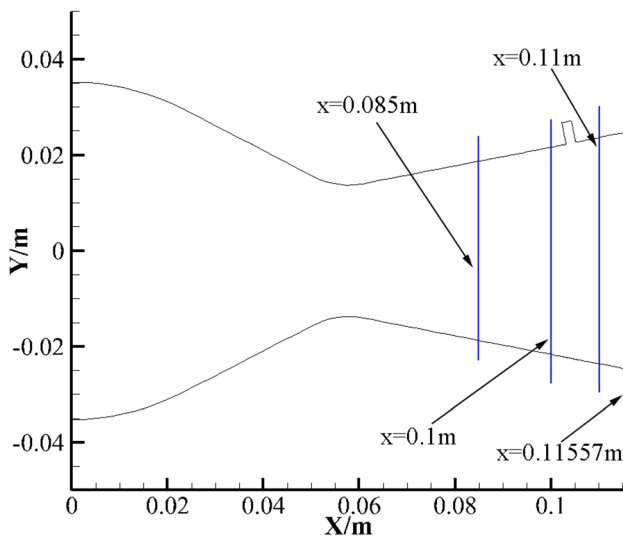

Fig. 5 Specific position of the y–z plane

near the boundary layer of the sidewall circled by an ellipse, which is due to the weak intensity of the separation shock wave generated by the separation of the sidewall boundary layer. Thus, the momentum loss of the primary flow near the wall is minimal, and it can continue to expand and accelerate rapidly. The primary flow in the middle part flows through the induced shock wave with high intensity, and the velocity decreases sharply; a remarkable difference in velocity between the two sections is observed. The zoom-in counterclockwise vortex encircled by a red wire frame is generated at the junction of the upper wall and the sidewall in Fig. 6d. This vortex enhances the entrainment of the wake into the surrounding atmosphere.

Figure 7 shows the Mach number distribution of the wake of the thrust vectoring nozzle. The nozzle's wake shows continuous entrainment to the surrounding atmosphere along the X axis, and its shape gradually changes. The existence of the counterclockwise vortex in Fig. 6d enhances the entrainment of the wake to the surrounding atmosphere, which leads to the gradual deepening of the upper side convex of the nozzle. The convex of the nozzle wake's left and right sides is due to the separation of the boundary layer caused by the induced shock wave. After $x=0.18$ m, various features of the wake gradually disappear with the loss of vorticity. It can be seen from Figs. 6 and 7, that there is a boundary effect, but this effect does not have a remarkable impact on the primary flow structure.

Figure 8 shows that the shape of the separation region in front of the secondary flow injection port varies along the Z-axis, which is the reason for the "wavy" Mach number distribution from Fig. 6b to d. However, the 3D effect of the flow is weak and has no essential effect on the structural change of the flow field. Therefore, the flow on the symmetrical surface can be chosen as the representative to further analyze the structural characteristics of the flow field.

To better understand the flow structure of the nozzle's flow field, the distribution and variation in Mach number and pressure coefficient of the nozzle's flow field in one cycle are analyzed. The cycle depends on the frequency of the first-order mode, $f_1 = 512.8$ Hz, which is given in Sect. 4.3. Figure 9 shows the Mach number distribution at $Z=0$. With the time development of flow, the area of the triangular recirculation region among the secondary flow, the primary flow, and the upper wall surface is constantly changing. Close examination of the separation region reveals that the x-scale decreases from T/6 to 2 T/6. From 3 T/6 to 5 T/6, the x-scale of the separation region resumes to be similar to that of T/6, but the depth decreases continuously. For T, the depth of the separation region increases, which is about to be resumed to be similar to that of T/6. Affected by the above phenomena, the position of the separation shock wave changes and its intersection with the upper wall moves back and forth. The swing of the upper and lower shear layers of the wake is also due to the continuous change in the scale and shape of the separation region. In Fig. 9, the horizontal positions of the circles of the upper and lower shear layers are same, with the development of time, the distance between the two shear layers changes constantly. The scale of the separation region at the lip of the upper wall is larger than that of the lower wall, and the flow structure becomes more complicated. The swing angle of the upper shear layer is significantly larger than that of the lower shear layer. Given the change in separation shock wave position in the nozzle, the positions of the shock wave and the expansion wave reflected along with the shear layer in the wake also change.
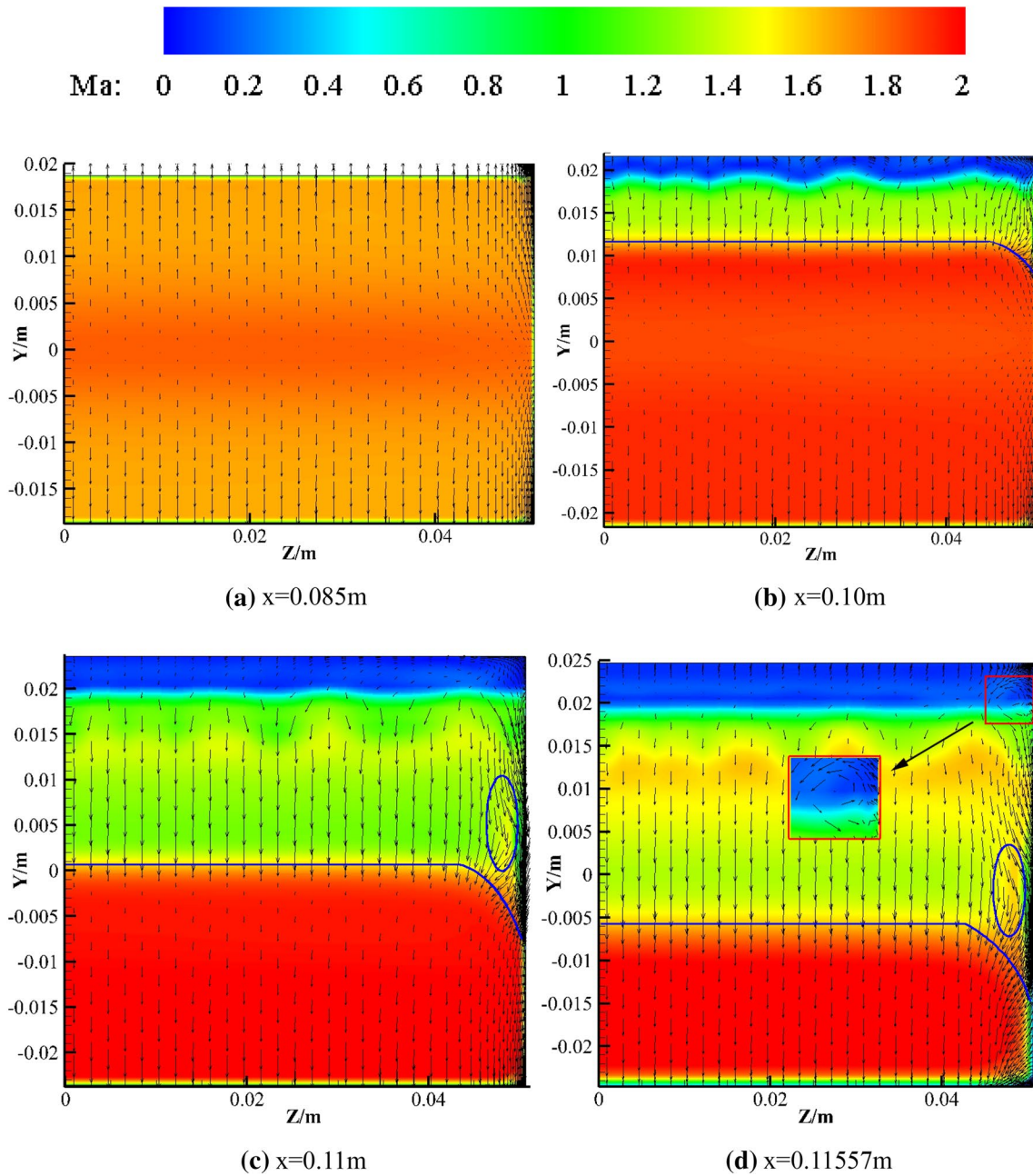
The pressure coefficient is defined as

(a) x=0.085m

(b) x=0.10m

(c) x=0.11m

(d) x=0.11557m

Fig. 6 Flow field distribution in the 1/2 *y*–*z* section

$$C_P = \frac{P - P_{\text{in}}}{\frac{1}{2}\rho_{\text{in}}v_{\text{in}}^2},\tag{8}$$

where P_{in} is the static pressure of the nozzle primary flow's inlet, ρ_{in} is the fluid density of the nozzle primary flow's inlet, and v_{in} is the velocity of the nozzle primary flow's inlet. Figure 10 shows the distribution of C_p of the nozzle's flow field. The flow in the nozzle convergent section and

throat are unaffected by secondary flow and separation shock due to the supersonic state in the diffusion section. Thus, a stable high-pressure coefficient is maintained. The red-blue interface of the nozzle diffusion section is where the separation shock wave is located. The position of the red-blue interface changes with time, proving that the separation shock wave oscillates in the flow field. The flow field is accompanied by pressure oscillations. The shear layers are
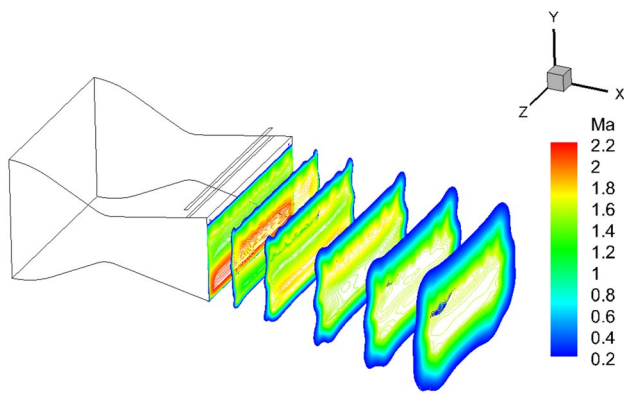
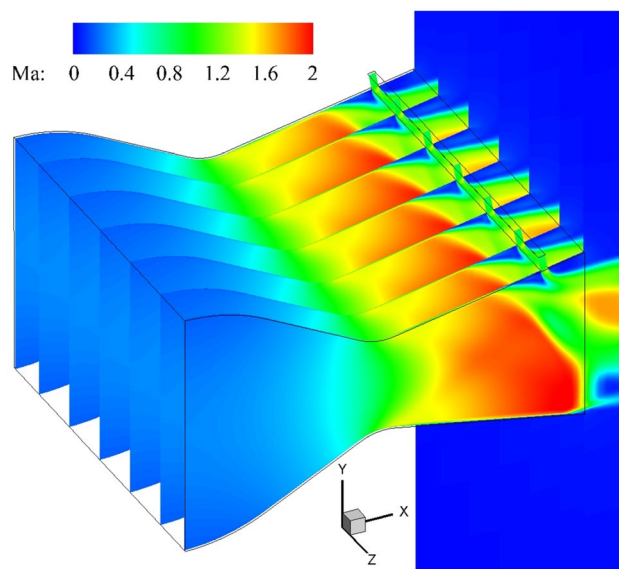**Fig. 7** Mach number distribution in the nozzle wake

Fig. 8 Mach number contour along Z-axis

composed of vortices. Figure 10 clearly shows the pressure oscillation of the wake, and the shedding of vortices in shear layers. The spatial scale of the vortices changes continuously during the shedding process. Using the vortex surrounded by the red wireframe as an example, the spatial scale of vortex increases from 1 T/6 to 3 T/6.

To capture vortices more clearly, the vector-lines based on (U_X, U_Y) is introduced, as shown in Fig. 11, where U_X is X-velocity component, U_Y is the Y-velocity component. The resultant velocity U_{XY} is defined as

$$U_{XY} = \sqrt{(U_X)^2 + (U_Y)^2}. \tag{9}$$

The vortices generated by the shear layers can be observed from Fig. 11. With the time development of flow, the vortices shed and shift downstream in the upper and lower shear layers.

The above-mentioned analysis demonstrates that the oscillating flow field will inevitably cause high aerodynamic noise, so the sound pressure level (SPL) of the flow field must be calculated. Figure 12 presents the overall sound pressure level distribution at Z = 0. The SPL upstream of the shock wave in the nozzle's expansion section is about 110 dB. The SPL around the shear layer of the wake and shock wave is very high. The SPL around the shear layer and oblique shock wave is about 130 dB and that around the "λ" shock wave peaks at 135 dB. The pressure fluctuation of flow field increases with the injection of secondary flow, and this strong fluctuation affects the thrust vectoring performance of the flow field and amplifies the noise of the wake. Therefore, further analysis on the oscillating flow field is necessary to explore the potential flow information. FMD technology is used to analyze the mechanism underlying high noise in the nozzle flow field in the following section.

4.3 Spectrum Analysis of FMD

The pressure coefficients of 2301 continuous flow fields on the nozzle's symmetrical surface are extracted for FMD analysis. Figure 13 illustrates the amplitude versus frequency of the flow field after FMD processing. The abscissa represents the frequency of the flow field, whereas the ordinate represents the amplitude of the pressure coefficient. Different amplitudes reveal the energy of varying modes in the flow field. Referring to reference [15], the frequencies corresponding to the three modes of the flow field are $f_1 = 512.8$ Hz, $f_2 = 2825$ Hz, and $f_3 = 4650$ Hz. 512.8 Hz is the first peak low-frequency, which is selected as the first-order frequency. 2825 Hz is the highest peak frequency, and the contribution of this mode to flow field is greatest among modes around 2825 Hz, so 2825 Hz is selected as the second-order frequency. 4650 Hz is next peak high-frequency relatively, which is selected as the third-order frequency. A comparison of the peak amplitude of the three modes reveals that the flow structure of the second-order mode has the highest oscillating energy, followed by that of the first-order mode. The third-order mode energy has the lowest oscillating energy among the three modes.

Digital elevation model (DEM) is used to show the amplitude variation of every mode on the nozzle's symmetrical surface. DEM is used often in geographic information systems, and are the most common basis for digitally-produced relief maps. In this paper, the amplitude of C_p is similar to the altitude of terrain model in geography. Figure 14 presents
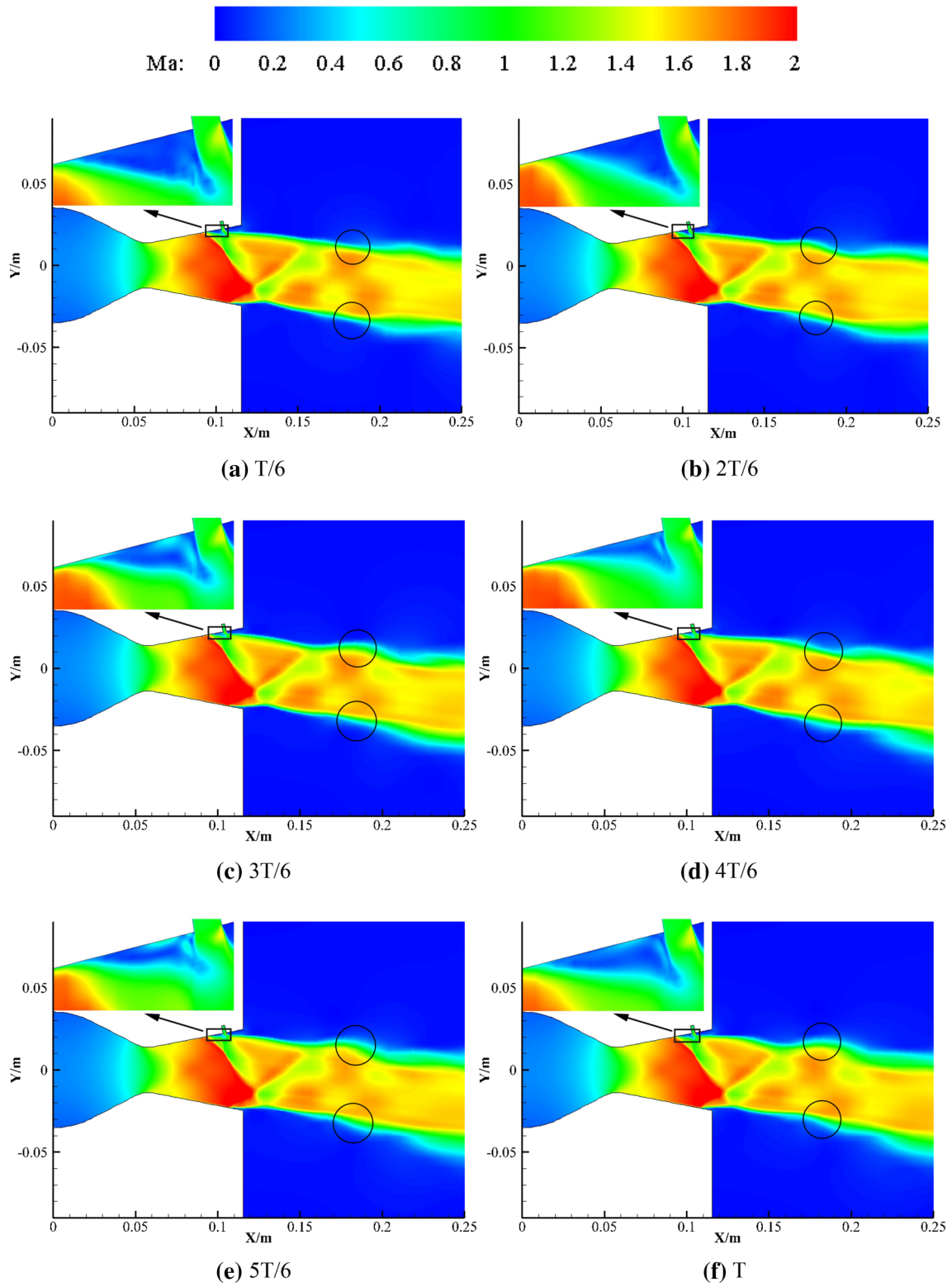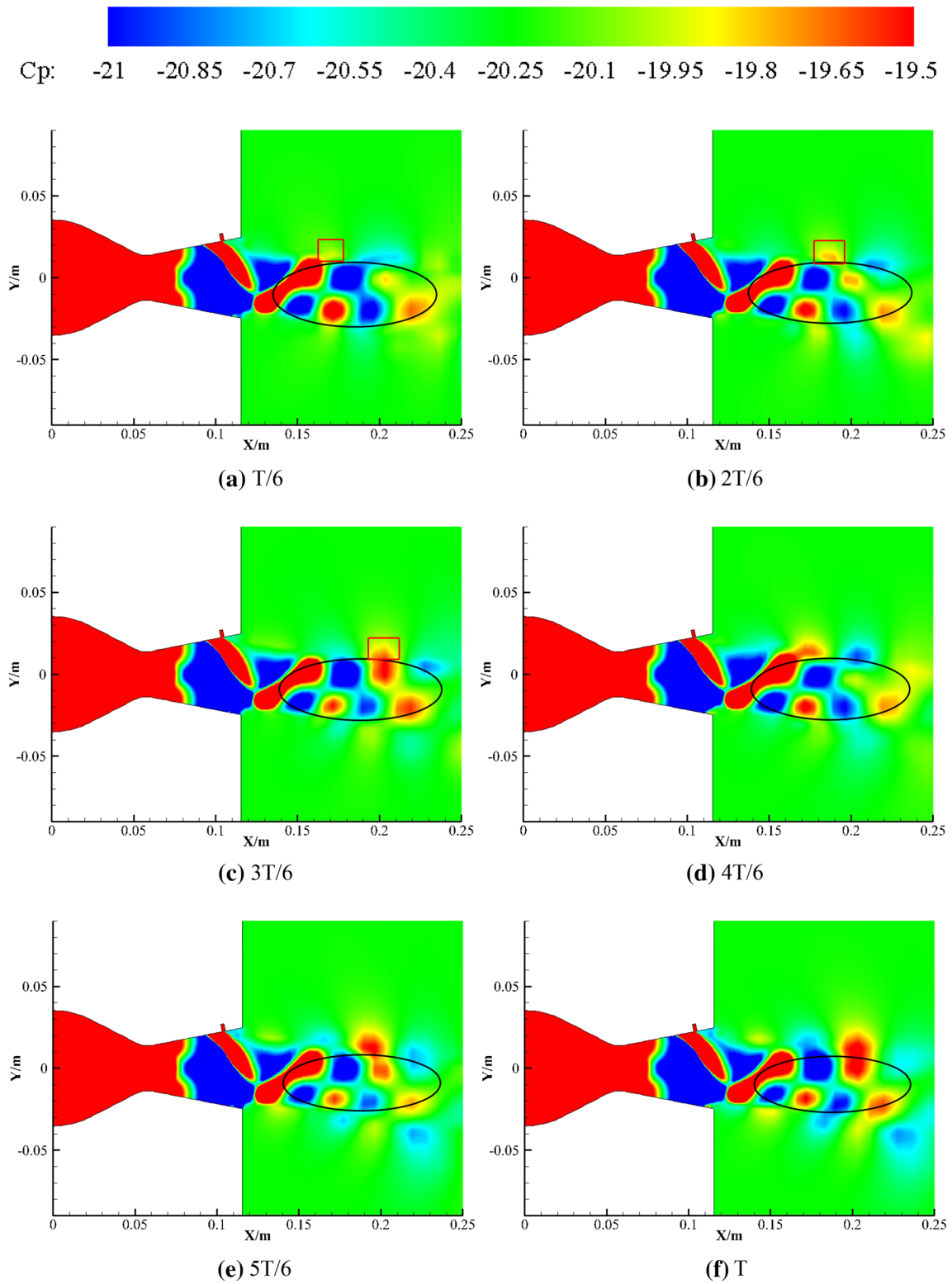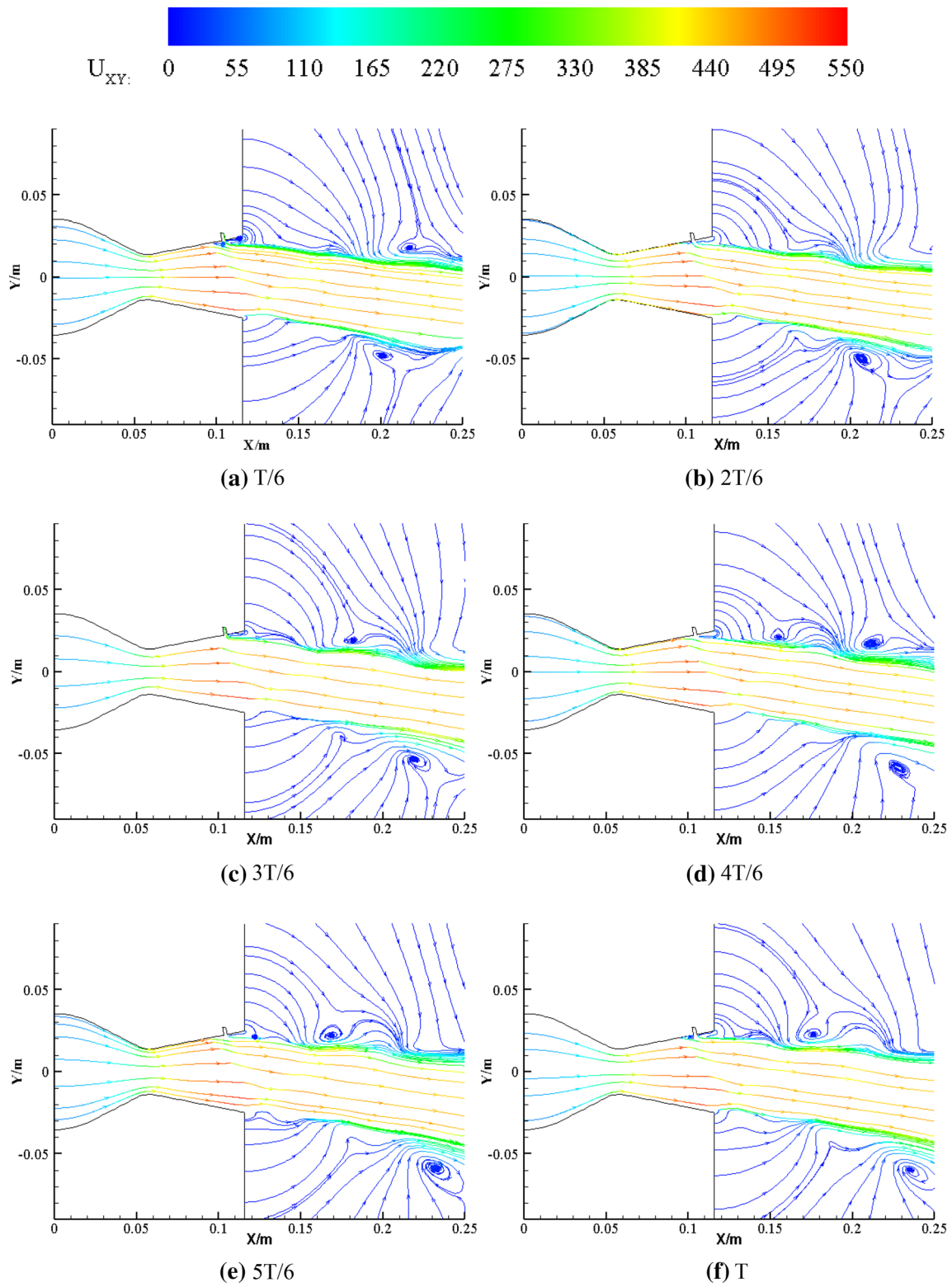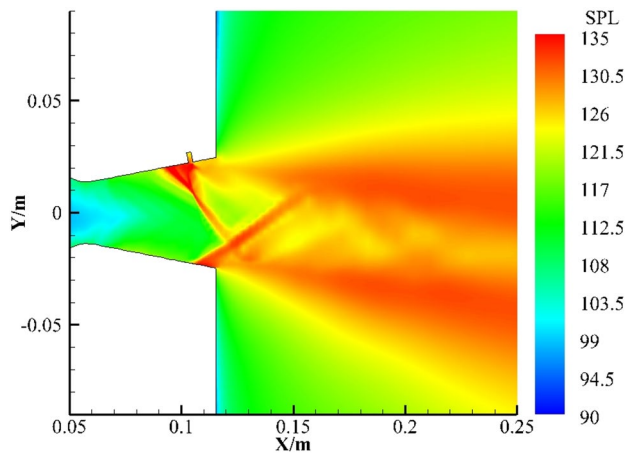
Fig. 9 Mach number distribution at $Z=0$
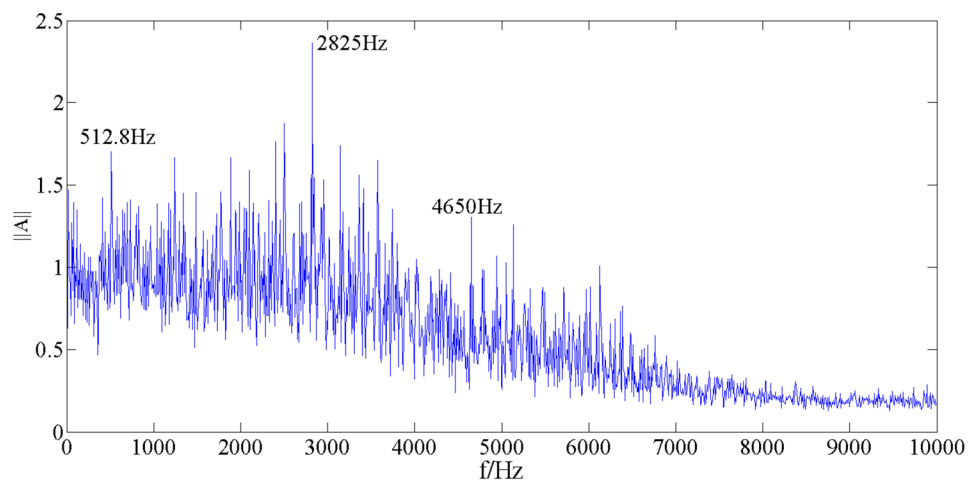
Fig. 10 Pressure coefficient distribution at $Z=0$

Fig. 11 Vector-lines based on (Ux, Uy) distribution at $Z=0$

Fig. 12 Overall sound pressure level distribution at $Z=0$

two common characteristics of the three modes of amplitude. One is that the amplitude of the "λ" shock wave of the entire flow field becomes prominent in fluctuation. The energy at the shock wave position accounts for a high proportion of the energy in the whole flow field. The other is that the amplitude along the X axis decreases with the development of the flow. The difference among the three modes is that the shock wave's amplitude of the first-order mode is higher than those of the other two modes. The second-order mode has lower amplitudes near the shock waves compared with the first-order mode, but the oscillation amplitude of the shear layers is higher and the spatial range of distribution is larger. Compared with the other two modes, the pressure oscillation of the shock wave and wake in the third-order mode is the weakest. The energy of the first-order mode is mainly concentrated on the shock waves, whereas the energy of the second-order mode is concentrated on the shock waves and shear layers.

4.4 Mean Flow Mode

Figure 15 shows the pressure coefficient distribution of the mean flow mode. The mean flow mode is the basic structure of the original time-average flow field. The location of the separation shock wave can be observed in this mode. The regions of different pressures divided by compression waves and expansion waves reflected on the shear layers can also be identified in the wake.

4.5 FMD Mode 1

The original flow field can be restored by superposing all FMD modes with mean flow modes, so the FMD mode represents the fluctuation in the flow field corresponding to each frequency. To capture the flow characteristics and rules of the nozzle flow field more clearly, the flow field of the first-order mode is evolved in the time domain. Figure 16 exhibits the pressure coefficient distribution of different phase flow fields on the nozzle symmetrical surface. The existence and fluctuation of the "λ" shock wave and the oblique shock wave can be clearly seen in the figure. Pressure fluctuations of the separation shock wave and induced shock wave are always opposite. Pressure fluctuation around the shock wave is not synchronized. In phase 1, about one-third scale of the separation shock wave has a negative fluctuation in pressure, and the pressure of the entire oblique shock wave is negatively fluctuating. In phase 2, the negative fluctuation in pressure has spread to the entire separation shock, and the pressure fluctuation range of the oblique shock is reduced to one-half of the entire shock. From phase 3 to phase 5, the pressure of the separation shock wave becomes positive fluctuation, and the range of fluctuation gradually extends to the whole separation shock wave. The oblique shock becomes positive fluctuation. The pressure coefficient distribution of phase 6 and phase 1 are similar, and the flow field completes
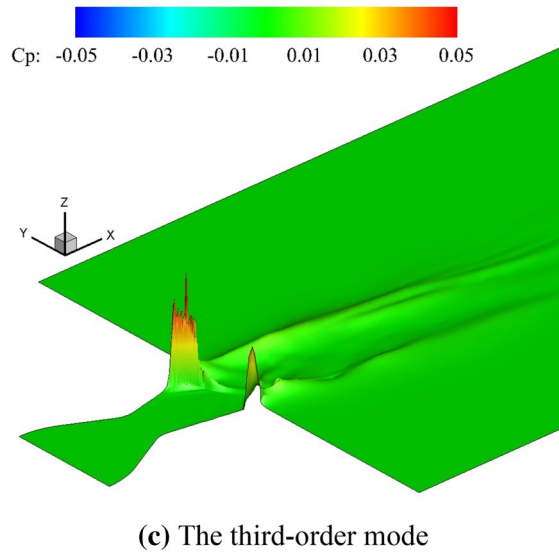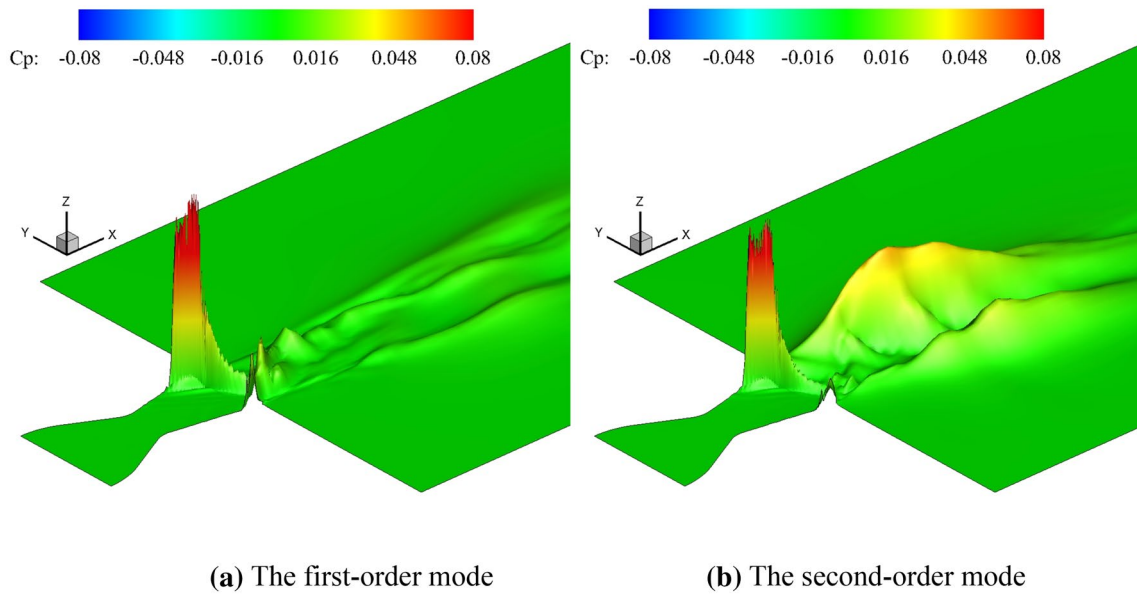
Fig. 13 FMD amplitude versus frequency

(a) The first-order mode

(b) The second-order mode

(c) The third-order mode

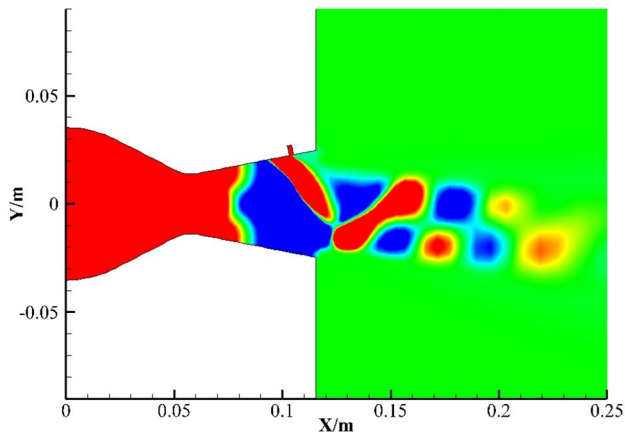**Fig. 14** Amplitude contours from the DEM for the three modes

Fig. 15 Pressure coefficient distribution of the mean flow mode

a cycle of flow. The first-order mode is mainly represented by the pressure fluctuation around the shock waves.

4.6 FMD Mode 2

The pressure coefficient distribution in the second-order mode shown in Fig. 17 can be obtained by evolving the pressure field of the second-order mode in the time domain. A notable difference between the first-order mode and second-order mode is observed. The second-order mode does not show the complete shock wave's oscillation, and the main changes appear in the shear layers of

(a) Phase1

(b) Phase2

(c) Phase3

(d) Phase4

(e) Phase5

(f) Phase6
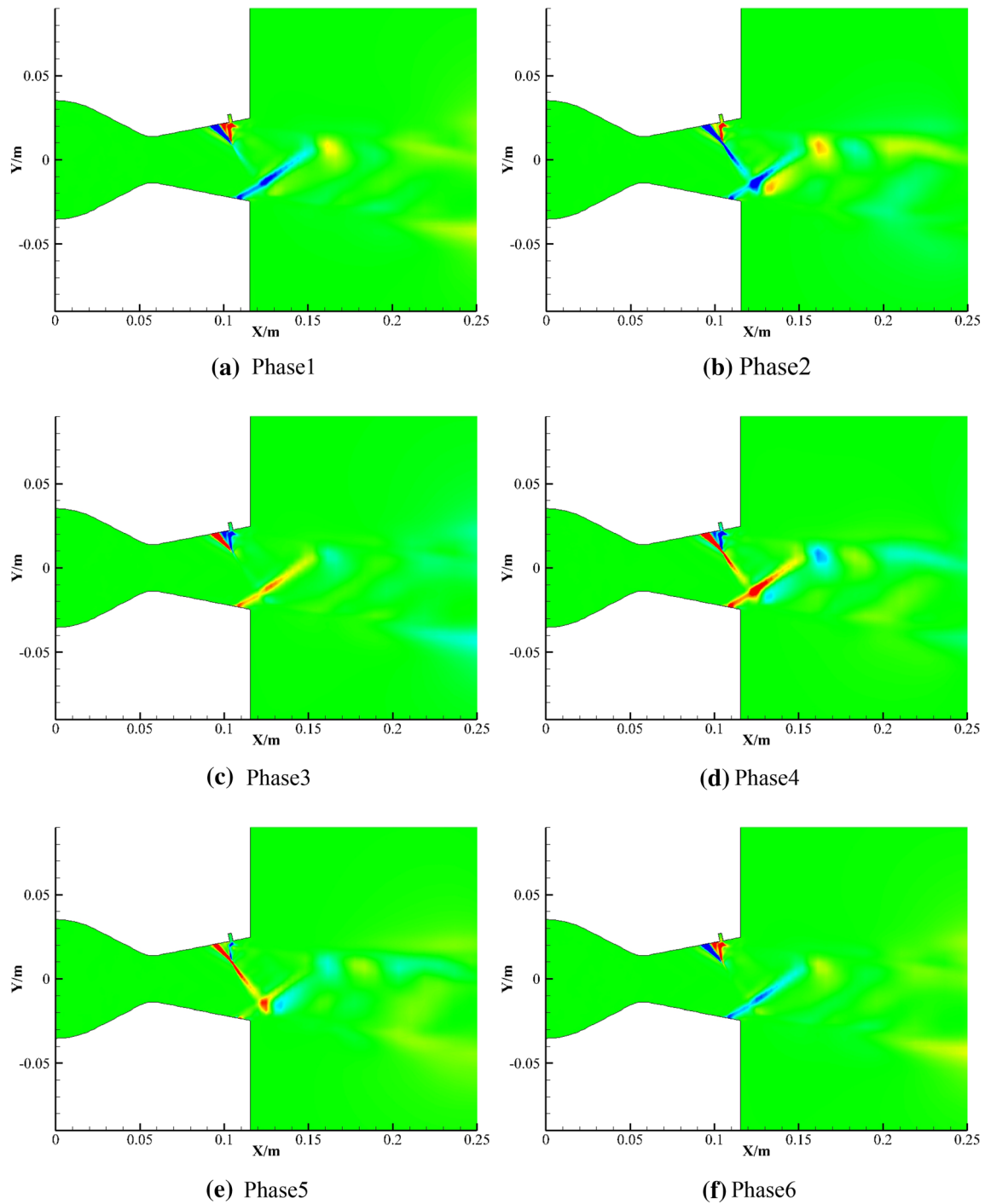
Fig. 16 Pressure coefficient contour of the first FMD mode

the wake. In Fig. 17, the vortices shed downstream along with the upper and lower shear. The fluctuation of the pressure coefficient between adjacent vortices is the opposite, and the spatial scale of vortices in the upper shear layer is obviously larger than that in the lower shear layer. The vortex's shedding process is described using the Vortex1 marked in Fig. 17. In phase 1, Vortex1 is located at $x = 0.16$ m. In phase 2, Vortex1 is spread at $x = 0.17$ m, and

(a) Phase1

(b) Phase2

(c) Phase3

(d) Phase4

(e) Phase5
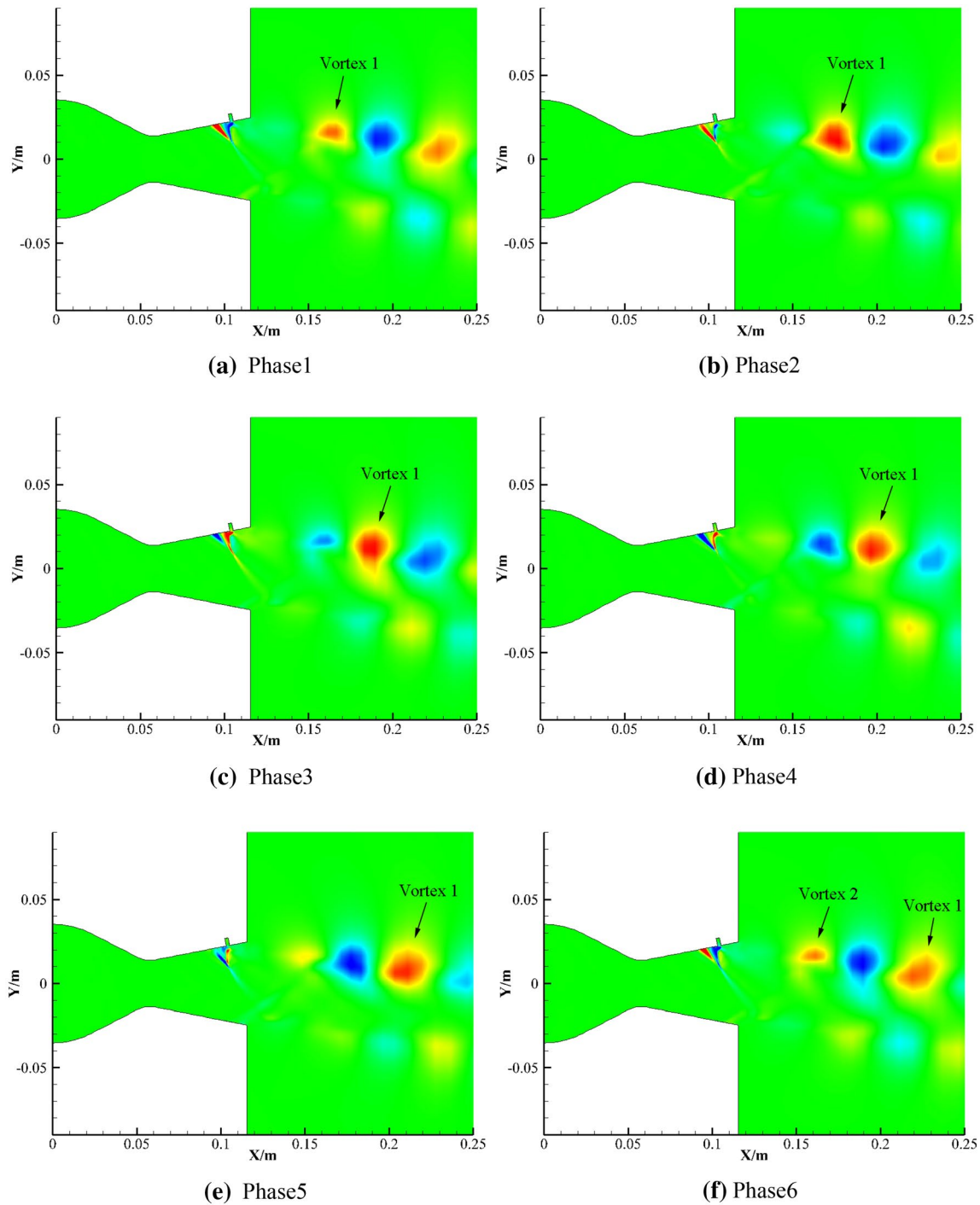
(f) Phase6

Fig. 17 Pressure coefficient contour of the second FMD mode

its spatial scale increases. In phases 3 to phase 4, Vortex1 moves from $x = 0.185$ m to $x = 0.2$ m. In phases 5, Vortex1 is located at $x = 0.21$ m. In phase 6, Vortex1 moves to $x = 0.23$ m. At the same time, a new Vortex 2 moves to the position of Vortex 1 in phase1. The flow fields of phase 1 and phase 6 are similar, and the flow completes a cycle. The main feature of the second-order mode is the shedding of the vortices in the shear layers.
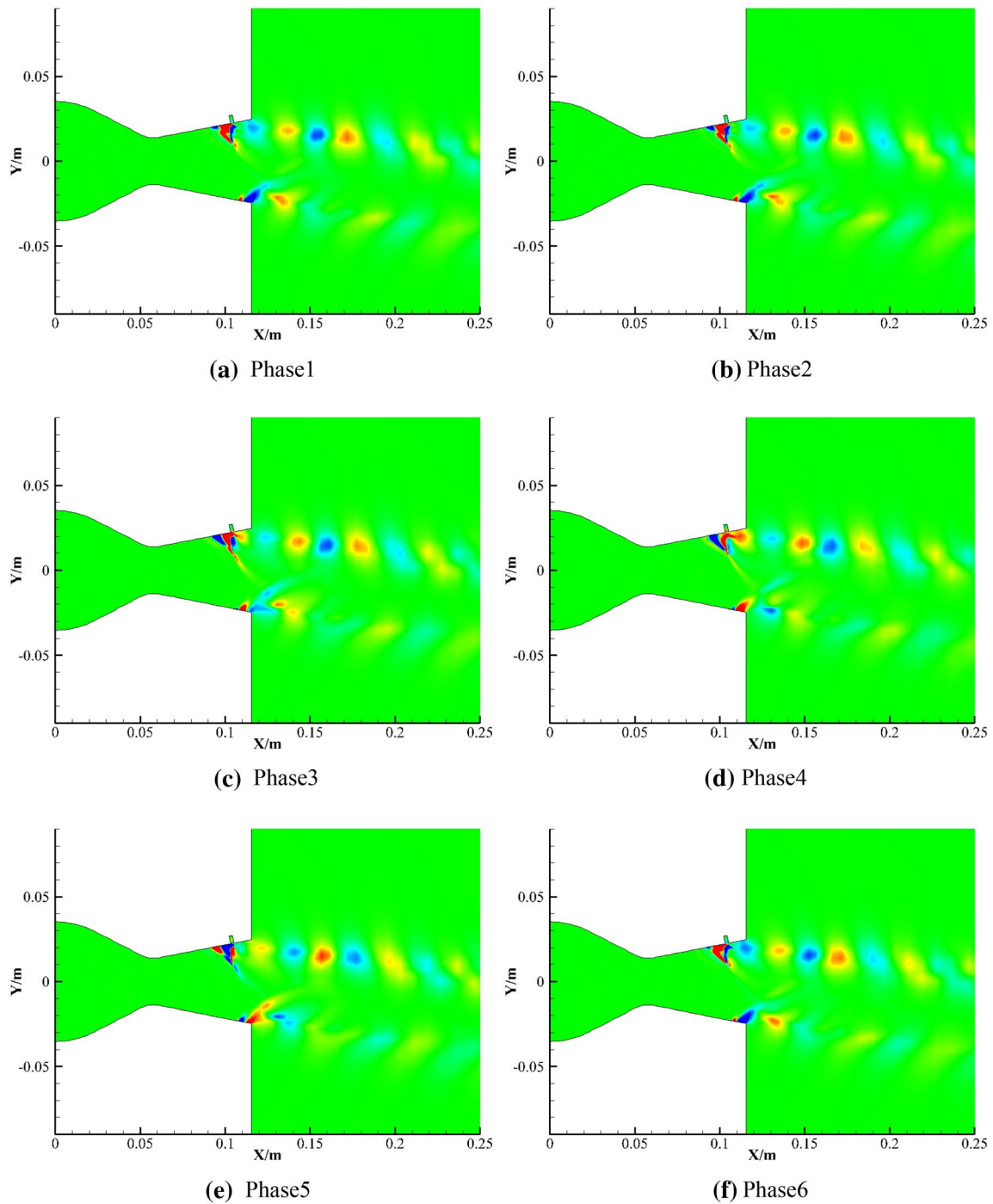
Fig. 18 Pressure coefficient contour of the third FMD mode

4.7 FMD Mode 3

Figure 18 shows the pressure coefficient distribution of the third-order mode with time. The evolution of the third-order mode is similar to that of the second-order mode. They all show the shedding of vortices, but the scale of the vortices of the third-order modes decreases and the number of vortices increases. The third-order modes show that the higher-order vortices begin to shed at the nozzle's wall.

5 Conclusions

The unsteady flow field of a single injection port fluidic thrust vectoring nozzle is numerically simulated using DES in this paper. The flow characteristic in the vector nozzle is studied, and the pressure coefficient of the nozzle symmetry plane is analyzed by FMD.

Given the existence of secondary flow, a "λ" shock wave formed by the separation shock wave and induced shock wave is generated in the nozzle, and vector deflection occurs when primary flow passes through the shock wave. Pressure at the shock waves oscillates with the time development of flow. At the same time, the vortices occur in the shear layer, which shed downstream. The swing angle of the upper shear layer is larger than that of the lower shear layer. The analysis of sound pressure level shows that the pressure oscillation of the flow field leads to high noise. FMD analysis shows three dominant natural modes in the flow field. The three frequencies are 512.8, 2,825, and 4,650 Hz. The first-order mode represents the pressure fluctuation of shock waves. The second-order mode represents the shedding of the vortices in the shear layers. The third-order mode is similar to the second-order mode, but the number of vortices increases and the spatial scale decreases.

References

1. Ferlauto M, Marsilio R (2018) Computational Investigation of Injection Effects on Shock Vector Control Performance. In: 2018 Joint Propulsion Conference, Cincinnati, Ohio, AIAA 2018–4934
2. Mason MS, Crowther WJ (2004) Fluidic thrust vectoring for low observable air vehicles. In: 2nd AIAA Flow Control Conference, Portland, Oregon, AIAA 2004–2210
3. Williams RG, Vittal BR (2002) Fluidic Thrust Vectoring and Throat Control Exhaust Nozzle. In: 38th AIAA/ASME/SAE/ASEE Joint Propulsion Conference and Exhibit, Indianapolis, Indiana, AIAA 2002–4060
4. Ivison W, Hambidge C, McGilvray M, et al (2019) Fundamental experiments of fluidic thrust vectoring for a hypersonic vehicle. In: AIAA Scitech 2019 Forum, San Diego, California, AIAA 2019–1680
5. Rakesh RB, Varghese S (2018) Fluidic Thrust Vectoring of Engine Nozzle. Proceedings of the International Conference on Modern Research in Aerospace Engineering, Lecture Notes in Mechanical Engineering: 43–51
6. Flamm JD, Deere K, Mason ML, et al (2006) Design enhancements of the two-dimensional, dual throat fluidic thrust vectoring nozzle Concept. In: 3rd AIAA Flow Control Conference, San Francisco, California, AIAA 2006–3701
7. Heo JY, Yoo KH, Lee Y, et al (2009) Fluidic Thrust Vector Control of Supersonic Jet Using Co-flow Injection. In: 45th AIAA/ASME/SAE/ASEE joint propulsion conference and exhibit, Denver, Colorado, AIAA 2009–5174
8. Neely AJ, Gesto FN, Young J (2007) Performance studies of shock vector control fluidic thrust vectoring. In: 43rd AIAA/ASME/SAE/ASEE Joint propulsion conference and exhibit, Cincinnati, OH, AIAA 2007–5086
9. Deng R, Setoguchi T, Kim HD (2016) Large eddy simulation of shock vector control using bypass flow passage. Int J Heat Fluid Flow 62:474–481
10. Giuliano VJ, Wing DJ (1997) Static investigation of a fixed-aperture nozzle employing fluidic injection for multiaxis thrust vector control. In: 33rd Joint Propulsion Conference and Exhibit, Seattle,WA
11. Wing DJ, Giuliano VJ (1997) Fluidic Thrust Vectoring of an Axisymmetric Exhaust Nozzle at Static Conditions. In: 1997 ASME Fluids Engineering Division Summer Meeting, United States
12. Deere KA (2000) Computational Investigation of the Aerodynamic Effects on Fluidic Thrust Vectoring. In: 36th AIAA/ASME/SAE/ASEE Joint Propulsion Conference & Exhibit, Hampton, VA AIAA 2000–3598
13. Waithe KA, Deere KA (2003) Experimental and Computational Investigation of Multiple Injection Ports in a Convergent-Divergent Nozzle for Fluidic Thrust Vectoring. In: 21st Applied Aerodynamics Conference, Orlando, Florida, AIAA 2003–3802
14. Mangin B, Chpoun A, Jacquin L (2006) Experimental and numerical study of the fluidic thrust vectoring of a two-dimensional supersonic nozzle. In: 24th Applied Aerodynamics Conference, San Francisco, California, AIAA 2006–3666
15. Ma LQ, Feng LH, Pan C et al (2015) Fourier mode decomposition of PIV data. Sci China Technol Sci 58(11):1935–1948
16. Saravanan V, Ko J, Lee S (2019) Conceptual Aerodynamic Design of Pintle Nozzle for Variable-Thrust Propulsion. Int. J. Aeronaut. Space Sci: pp 1–14
17. Lee JH, Han YO (2019) Numerical investigation on evolution of tip vortices generated by low-aspect ratio rectangular wings at high angle of attack. Int J Aeronaut Space Sci 20(1):44–56
18. Choi H, Cho J (2019) Aerodynamic analysis and parametric study of the blended-wing-body-type business jet. Int J Aeronaut Space Sci 20(2):335–345
19. Casadei L, Könözsy L, Lawson NJ (2019) Unsteady Detached-Eddy Simulation (DES) of the Jetstream 31 aircraft in One Engine Inoperative (OEI) condition with propeller modelling. Aerosp Sci Technol 91:287–300
20. Spalart PR, Jou WH, Strelets M, et al (1997) Comments on the Feasibility of LES for Wings, and on a Hybrid RANS/LES Approach. In: 1st Air Force Office of Scientific Research International Conference on DNS/LES, Ruston, LA
21. Strelets M (2001) Detached eddy simulation of massively separated flows. In: 39th AIAA Aerospace Sciences Meeting and Exhibit, Reno, NV, AIAA 2001–0879
22. Menter FR, Kuntz M, Langtr R (2003) Ten years of industrial experience with the SST turbulence mode. Turbulence Heat Mass Transf 4(1):625–632
23. Wang JM, Ming XJ, Wang H et al (2018) Dynamic mode decomposition of a wing-body junction flow. Fluid Dyn 53(3):442–451
24. Wang JM, Ming XJ, Wang H et al (2019) Flow characteristics of a supersonic open cavity. Fluid Dyn 54(5):724–738